Ceramics International 42 (2016) 11743–11756

Contents lists available at ScienceDirect

Ceramics International

journal homepage: www.elsevier.com/locate/ceramint

Structural and mechanical properties of NbN and Nb-Si-N films: Experiment and molecular dynamics simulations

Alexander D. Pogrebnjak [a,b,*], Oleksandr V. Bondar [a,b,*], Gregory Abadias [c], Volodymyr Ivashchenko [d], Oleg V. Sobol [e], Stefan Jurga [b,f], Emerson Coy [b]

[a] Sumy State University, R.-Korsakova 2, 40007 Sumy, Ukraine
[b] NanoBioMedical Centre, Adam Mickiewicz University, ul. Umultowska 85, 61614 Poznań, Poland
[c] Institut Pprime, Université de Poitiers-CNRS-ENSMA, 86962 Futuroscope-Chasseneuil Cedex, France
[d] Institute of Problems of Material Science, NAS of Ukraine, Krzhyzhanovsky 3, 03680 Kyiv-142, Ukraine
[e] National Technical University "KhPI", Kharkiv, ul. Frunze, 21, 61002 Kharkiv-2, Ukraine
[f] Department of Macromolecular Physics, Adam Mickiewicz University, ul. Umultowska 85, 61614 Poznań, Poland

ARTICLE INFO

Article history:
Received 11 April 2016
Received in revised form
17 April 2016
Accepted 18 April 2016
Available online 19 April 2016

Keywords:
Nitrides
Films
Hardness
Mechanical properties
Strength

ABSTRACT

The structural and mechanical properties of NbN and Nb-Si-N films have been investigated both experimentally and theoretically, in their as-deposited and annealed states. The films were deposited using magnetron sputtering at substrate bias (U_B) between 0 and −70 V. While NbN films were found to crystallize in the cubic δ-NbN structure, Nb-Si-N films with Si content of 11–13 at% consisted of a two-phases nanocomposite structure where δ-NbN nanocrystals were embedded in SiN_x amorphous matrix. Films deposited at U_B=0 V were highly (001)-textured. Application of substrate bias potential led to a depletion of light atoms, and caused a grain size refinement concomitantly with the increase of (111) preferred orientations in both films. The maximum hardness was 28 GPa and 32 GPa for NbN and Nb-Si-N films, respectively. NbN and Nb-Si-N films deposited at U_B=−70 V exhibited compressive stress of −3 and −4 GPa, respectively. After vacuum annealing, a decrease in the stress-free lattice parameter was observed for both films, and attributed to alteration of film composition. To obtain insights on interface properties and related mechanical and thermal stability of Nb-Si-N nanocomposite films, first principles molecular dynamics simulations of NbN/SiN_x heterostructures with different structures (cubic and hexagonal) and atomic configurations were carried out. All the hexagonal heterostructures were found to be dynamically stable and weakly dependent on temperature. Calculation of the tensile strain-stress curves showed that the values of ideal tensile strength for the δ-NbN(111)- and ε-NbN(001)-based heterostructures with coherent interfaces and Si_3N_4–like Si_2N_3 interfaces were the highest with values in the range 36–65 GPa, but lower than corresponding values of bulk NbN compound. This suggests that hardness enhancement is likely due to inhibition of dislocation glide at the grain boundary rather than interfacial strengthening due to Si-N chemical bonding.

1. Introduction

Due to the unique combination of metallic, covalent and ionic bonding character, transition metal nitrides offer exceptional multi-functional properties, which make them attractive for a wide range of applications in microelectronics, optoelectronics or cutting tool industry. Among them, NbN exhibit a variety of interesting properties like high melting point and high hardness, electrical conductivity, chemical inertness. Improved mechanical properties and thermal stability have been reported in NbN-based nanolayers compared to monolithic coatings [1]. NbN films are used as cathode material for field emission in vacuum microelectronic devices [2] and can be exploited as tunnel junctions due to their superconducting nature [3].

Nanostructured films [4–6] are widely used as wear-protection coating on cutting tools due to high hardness, good corrosion stability and low friction coefficient [7]. Among these films, nanostructured NbN-based films are of increasing interest. The hardness of such films is much higher than the bulk material (HV=14 GPa) and higher than other binary nitride films (TiN, ZrN, VN). The hardness of the NbN films deposited by different arc deposition systems reaches 34–49 GPa [8–13]. The NbN films were also prepared by using magnetron sputtering (MS) [14–18], ion

* Correspondence to: Department of Nanoelectronics, Sumy State University, R.-Korsakova Str., 2, 40007 Sumy, Ukraine.
E-mail addresses: alexp@i.ua (A.D. Pogrebnjak), oleksandr.v.bondar@gmail.com (O.V. Bondar).

http://dx.doi.org/10.1016/j.ceramint.2016.04.095
0272-8842/

beam assisted deposition [19], pulsed laser deposition [20]. An increase in hardness was reached by the formation of the nanocomposite or nanolayered structures in ternary Nb-Si-N films [21–29]. Silicon nitride is known for its high temperature stability, low friction coefficient and high oxidation resistance. Hence, one can expect that Nb-Si-N nanocomposite will combine the properties of the constituent materials and will have improved properties as compared to NbN. Recently the comprehensive review of the investigations on NbN and Nb-Si-N films deposited by magnetron sputtering was reported [30]. It was shown that the NbN system crystallizes in different structural phases: cubic δ-NbN (a small number of vacancies are present in both the sublattices, space group Fm-3m) and hexagonal ε-NbN (space group P-6 m2) and δ ′-NbN (space group $P6_3/mmc$), depending on deposition parameters. The formation of the hexagonal phases occurs at high nitrogen partial pressures and substrate biases [14–16,18]. The hardness of the hexagonal δ′ and ε phases of NbN is higher compared to that of the cubic δ-NbN [14,15]. The addition of silicon up to 3.4 at% led to an increase in hardness up to 53 GPa [21]. This hardness enhancement was due to the specific nanocomposite structure of Nb-Si-N films that represented nano-sized NbN grains embedded in amorphous SiN_x matrix [21–26]. An increase in hardness from 25 GPa to 34 GPa was explained in the framework of a two-step mechanism, i.e., by forming a solid solution of Si atom in NbN lattice and by forming a nanocomposite material [22–24]. The hardness of Nb-Si-N nanocomposite films reaches the maximum values of 30–34 GPa for 5–13 at% of Si [23]. As in the case of NbN, for the Nb-Si-N system, high substrate biases and nitrogen partial pressures promote the growth of the ε-NbN grains [25,26].

Despite extensive studies reported in the literature, the comparative evolution of NbN and Nb-Si-N films prepared at different substrate biases was not yet carried out. Moreover, previous simulations of NbN/SiN_x nanostructures were restricted to δ-NbN(001)/Si_3N_4 interfaces [30].

In this work we aimed to show a comprehensive report on the physical and chemical properties of the NbN and Nb-Si-N films and we close the gaps in the investigations of NbN and Nb-Si-N films. The films were deposited on silicon wafers at various substrate biases (U_B). The films were then investigated by an atomic force microscope (AFM), X-ray diffraction (XRD), X-ray photoelectron spectroscopy (XPS), wavelength and energy dispersive X-ray spectroscopy, nanoindentaion and microindentation. The deposited films were annealed in vacuum at 1000 °C at a pressure of 10^{-4} Pa to establish their thermal stability. NbN/SiN_x heterostructures were calculated at various temperatures using first-principles molecular dynamics simulations to interpret the experimental results on the Nb-Si-N films.

2. Experimental and computational details

2.1. Experiment procedures

NbN-based films were deposited on mirror-polished Si (100) wafers by DC reactive magnetron sputtering using Nb (99.9%, Ø72 × 4 mm) and Si (99.999%, Ø72 × 4 mm) targets in an argon-nitrogen atmosphere at the following deposition parameters: substrate temperature $T_S = 350$ °C; flow rate (F) $F_{Ar} = 40$ sccm; $F_{N2} = 13$ sccm; working pressure $P_C = 0.17$ Pa. The current applied to the Nb target was 300 mA, which corresponded to a discharge power density $P_{Nb} = 17.1$ W/cm^2. The current on the Si target was 100 mA ($P_{Si} = 5.3$ W/cm^2). Substrate biases were $U_B = 0, -20, -40, -50$ and -70 V. Base pressure inside the vacuum chamber was better than 10^{-4} Pa. The distance between the targets and the substrate holder was 8 cm. The dihedral angle between the target planes was ~45°. The substrates were cleaned ultrasonically before they were put into the vacuum chamber. Also, before deposition, the substrates were etched in the vacuum chamber in hydrogen plasma during 5 min Post-deposition vacuum annealing at 1000 °C was done using Pekly Herrmann Moritz JF1013 device (France) with PFEIFFER HiCube 80 Eco vacuum pump (Germany). The residual pressure in the furnace was 10^{-4} Pa.

The thickness of the films was determined with an optical profilometer "Micron-Gamma". The thickness of the films deposited during 50 min increased with increasing bias (U_B) from 0 to -70 V, from 0.6 to 0.8 μm (NbN films) and from 1.0 to 1.2 μm (Nb-Si-N films).

The crystal structure of the films was determined by X-ray diffraction (XRD, diffractometer DRON-3M) using CuK_α radiation. Broadening of XRD peaks from two reflections defined the size of crystallites and microstresses in coatings based on the method of Williamson-Hall. This method is easier than the Warren-Averbach method, but in the case of wide diffraction lines of the reflections of the second order it allows to receive more accurate results in defining of substructure characteristics, such as size of crystallites and micro-stresses. In order to define the stress-strain state of the NbN and Nb-Si-N coatings we used the $\sin^2\psi$ method [31]. This method gives reliable results either for macro-objects or for films and coatings and it allows to determine the stress-state state of each component phase. Stress measurements were performed on a four circle Seifert XRD diffractometer, operating at 40 mA and 40 kV, using point focus geometry with Cu X-ray source, a 1.0 mm diameter collimator, a Ni filter to absorb the Cu K_β wavelength and a scintillation detector [32]. Measurements were taken by recording 2θ scans of the cubic {200} NbN reflection at different specimen tilt angles ψ ranging from 0 to 88°.

The chemical bonding state of the films was analyzed by X-ray photoelectron spectroscopy (XPS, EC 2401, USSR) using MgK_α radiation (E = 1253.6 eV). The Au 4f7/2 and Cu 2p3/2 peaks with binding energy at 84.0 ± 0.05 eV and 932.66 ± 0.05 eV, respectively, were used as a reference. Prior to the XPS measurements, the samples were sputter-etched in argon plasma for 5 min.

Microstructure and element composition investigations were done using scanning electron microscope (SEM) JEOL-7001F-TTLS equipped with wavelength-dispersive X-ray spectroscopy (WDS) microanalysis unit from Oxford Instruments, while surface morphology was analyzed by atomic force microscope (AFM) Nano-Scope IIIa Dimension 3000 (Digital Instruments, USA). Cross-sectional transmission electron microscopy (XTEM) investigations were carried out in high resolution, bright-field, dark-field and selected area electron diffraction (SAED) modes using a JEOL-FS device equipped with a field-emission gun and an omega energy filter. A cross section of the Nb-Si-N sample, deposited at -70 V bias, was prepared by focused ion beam (JEOL JIB-4000) using a gallium ion source and acceleration voltage of 30 kV. The cross section was then studied by high-resolution transmission electron microscopy (HR-TEM, JEOL-ARM 200 F) with an accelerating voltage of 200 kV, equipped with an energy-dispersive X-ray spectroscopy (EDS) detector. Samples were placed by micromanipulator on a commercially available ultra-thin copper grid. The hardness and elastic modulus of films were determined from indentation by Nanoindenter-G200 instrument equipped with a Berkovich pyramidal tip under load in the range of 9–13 mN. This range of loads was chosen in order to obtain prominent plastic deformation of film while avoiding the influence of substrate material. The nanohardness (H) and elastic modulus (E) data were obtained from the load-displacement curves using Oliver and Pharr method.

2.2. Theoretical methods

We have considered hexagonal ε-NbN(001)/SiN_x and δ-NbN(111)/SiN_x heterostructures as representative interfaces in the NbN/SiN_x nanocomposite films, and studied their strength theoretically at 0 K and 1400 K in the framework of first-principles quantum molecular dynamics (QMD) calculations with subsequent static relaxation. The δ-NbN(001)/Si_3N_4 heterostructures were investigated in our previous work [30]. Nevertheless, we included the discussion on these interfaces to compare them with the heterostructures computed in this investigation. Both (001) and (111)-oriented heterostructures were examined since the Nb-Si-N films were found to exhibit either a (200) or (111) preferred grain orientation. Different chemical compositions and atomic configurations of the initial supercells used for the investigation of the heterostructures are reported in Table 1, including the case of coherent or non-stoichiometric interfaces.

Table 1
Notation, composition, ideal tensile strength (σ_T) and failure tensile strain (ε_T) for the bulk NbN and NbN/SiN_x heterostructures.

Initial interface	Notation	Composition	σ_T (GPa)	ε_T
δ-NbN(001) [bulk]	δ-NbN(001)	$Nb_{48}N_{48}$	31.7	0.16
δ-NbN(001)/coherent $Si_{0.75}N$	δ-Si_3N_4	$Nb_{40}N_{40}/Si_6N_8$	14.1	0.08
δ-NbN(111) [bulk]	δ-NbN(111)	$Nb_{27}N_{27}$	95.1	0.52
δ-NbN(111)/Si_3N_4-like Si_2N_3	δ-Si_2N_3	$Nb_{45}N_{45}/Si_6N_9$	35.5	0.18
δ-NbN(111)/Si_3N_4-like SiN	δ-SiN	$Nb_{27}N_{27}/Si_9N_9$	20.2	0.14
δ-NbN(111)/coherent SiN	δ-coherent SiN	$Nb_{18}N_{18}/Si_9N_9$	63.9	0.16
ε-NbN(001) [bulk]	ε-NbN(001)	$Nb_{36}N_{36}$	105.8	0.32
ε-NbN(001)/Si_3N_4-like Si_2N_3	ε-Si_2N_3	$Nb_{36}N_{36}/Si_6N_9$	47.2	0.12
ε-NbN(001)/Si_3N_4-like SiN	ε-SiN	$Nb_{27}N_{27}/Si_9N_9$	6.4	0.08
ε-NbN(001)/coherent SiN	ε-coherent SiN	$Nb_{27}N_{27}/Si_9N_9$	48.0	0.10

The QMD calculations were performed with the quantum ESPRESSO code [33] using periodic boundary conditions and the generalized gradient approximation (GGA) of Perdew, Burke and Ernzerhof (PBE) [34] for the exchange-correlation energy and potential. Vanderbilt ultra-soft pseudo-potentials were used to describe the electron-ion interaction [35]. The criterion of convergence for the total energy was 10^{-6} Ry/formula unit ($1.36 \cdot 10^{-5}$ eV/formula unit). In order to speed up the convergence, each eigenvalue was convoluted by a Gaussian with a width $\sigma = 0.02$ Ry (0.272 eV).

The initial structure was optimized by simultaneously relaxing the supercell basis vectors and the atomic positions inside the supercell using the Broyden-Fletcher-Goldfarb-Shanno (BFGS) algorithm [36]. The QMD calculations of the initial relaxed heterostructure were carried out at 1400 K with fixed unit cell parameters and volume (NVT ensemble, constant number of particles-volume-temperature) for 1.7 ps. In the QMD calculations, the time step was 20 a.u. (about 10^{-15} s). The system temperature was kept constant by rescaling the velocity, and the variation of the total energy was controlled during each QMD time step. All structures reached their time-averaged equilibrium during the initial calculation time of about 1 ps, and afterwards, the total energy of the

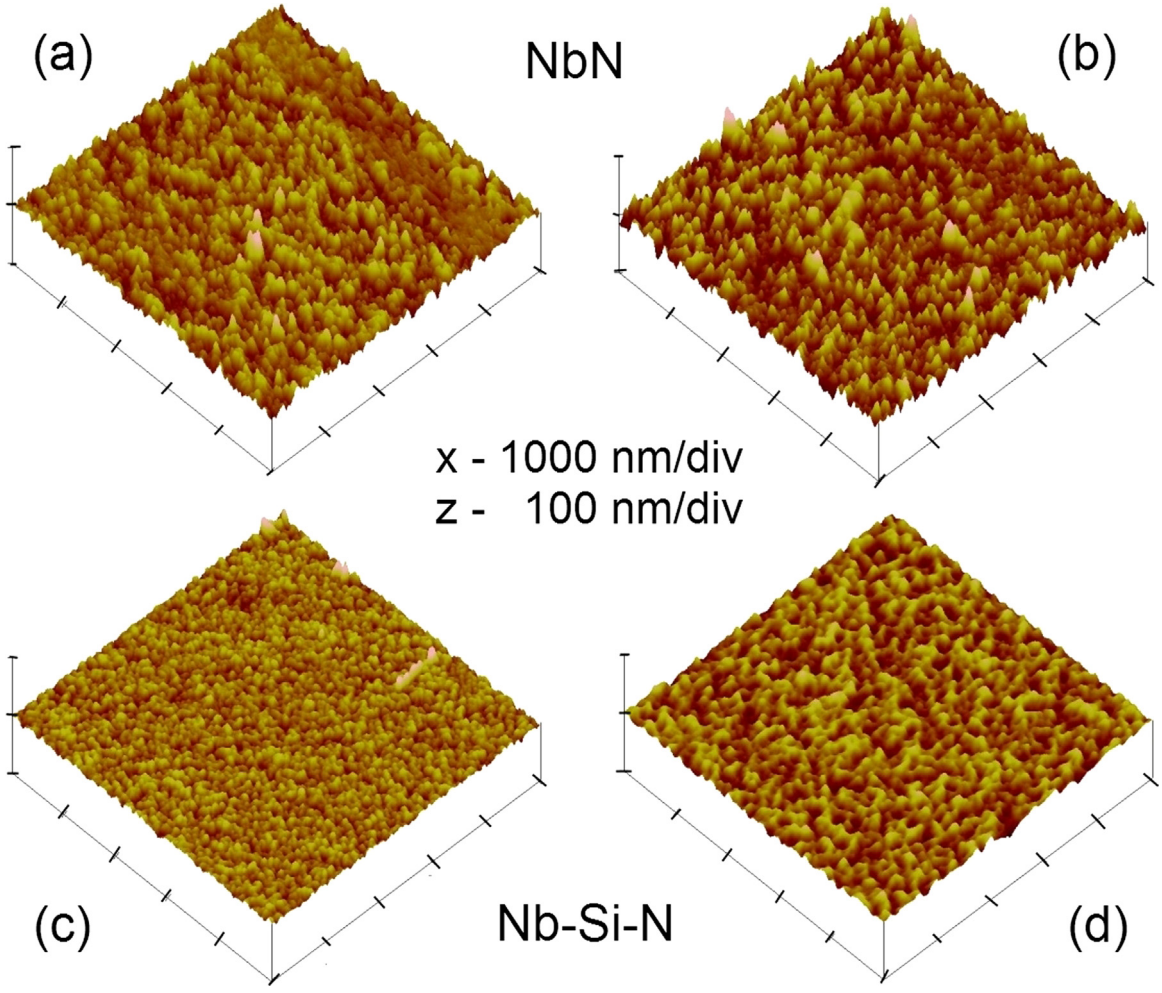

Fig. 1. AFM images for: the NbN films, deposited at $U_B = 0$ V (RMS = 6.4 nm) (a) and $U_B = -70$ V (RMS = 7.6 nm) (b); Nb-Si-N films, deposited at $U_B = 0$ V (RMS = 2.8 nm) (c) and $U_B = -70$ V (RMS = 3.6 nm) (d). The RMS roughness was determined at the area of 5 μm × 5 μm.

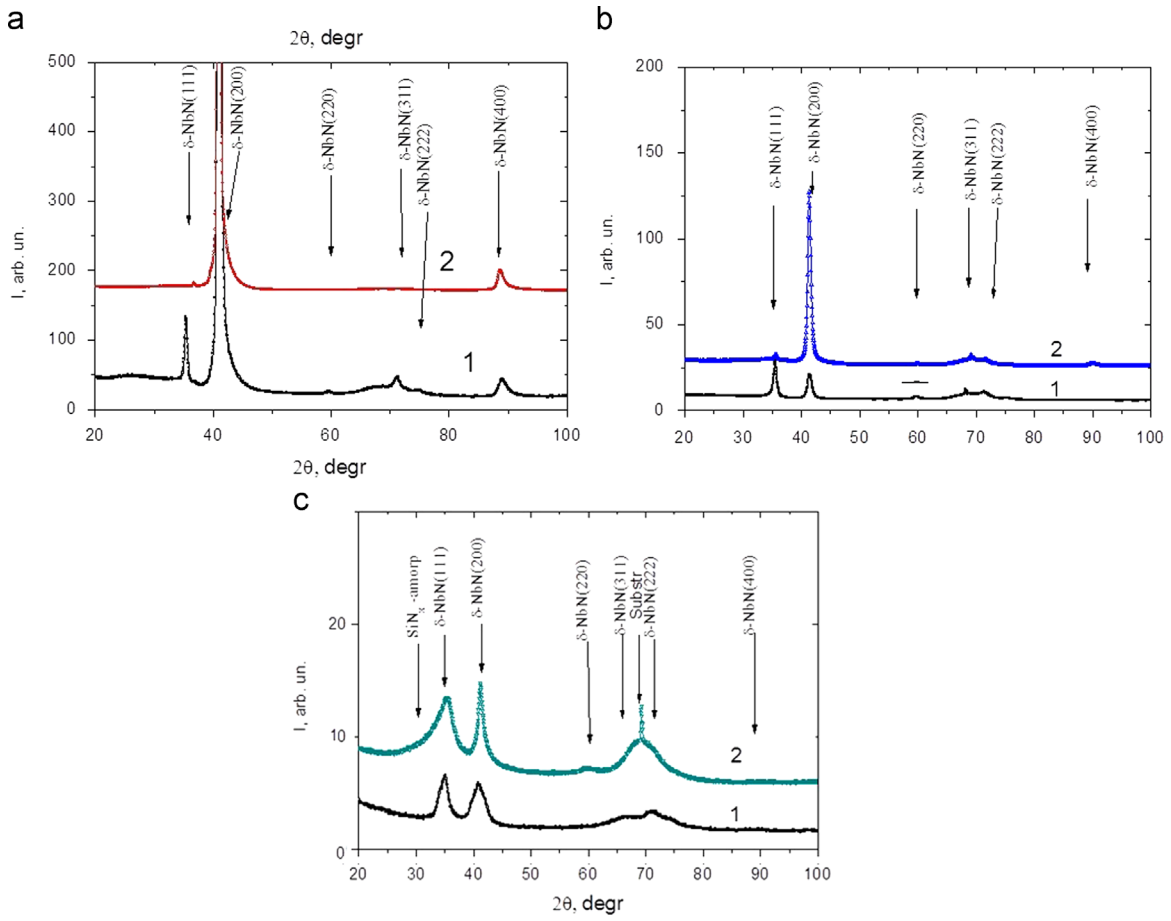

Fig. 2. XRD patterns for NbN (1) and Nb-Si-N (2) films prepared at $U_B = 0$ V (a), $U_B = -40$ V (b) and $U_B = -70$ V (c).

Table 2
Structural characteristics of NbN and Nb-Si-N coatings deposited at different bias voltage (U_B) and after vacuum annealing at T_{an}. D refers to the average grain size, $\langle\varepsilon\rangle$ to the average microstrain.

Coatings	U_B, V	T_{an}, °C	Main phases	D, nm	$\langle\varepsilon\rangle$, %	Axis of preferred orientation
NbN	0	–	δ-NbN	27	1.5	[100]
	−40	–	δ-NbN	86	2.1	Random
	−40	1000	δ-NbN	200	0.22	Random
	−70	–	δ-NbN	17	1.7	Random
	−70	1000	δ-NbN	87	0.45	Random
Nb-Si-N	0	–	δ-NbN	50	0.5	[100]
	0	1000	δ-Nb(Si)N	67	0.47	[100]
	−20	–	δ-NbN/Si_3N_4	47	0.5	[100]
	−40	–	δ-Nb(Si)N	27	0.5	[100]
	−40	1000	δ-Nb(Si)N	120	0.25	[100]
	−70	–	δ-NbN/SiN_x (amorph.)	9.1	0.6	Random
	−70	1000	δ-NbN/SiN_x	150	0.3	[100]

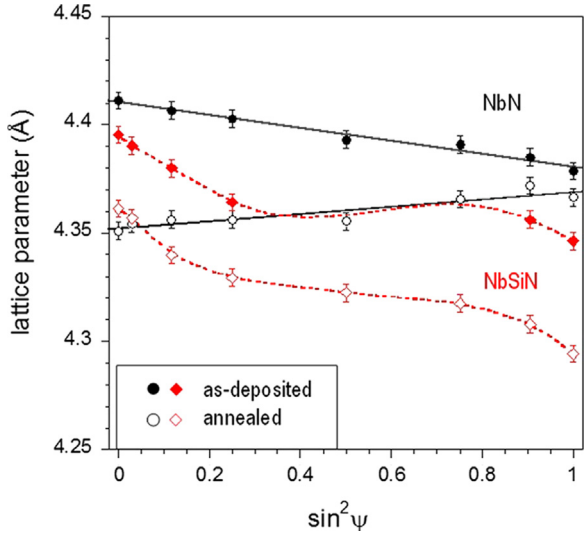

Fig. 3. $\sin^2\psi$ plot for the NbN and Nb-Si-N films deposited at $U_B = -70$ V before (shaded circles) and after (non-shaded circles) vacuum annealing.

structures fluctuated only slightly around that equilibrium value. In the large-scale QMD simulation, the chosen reduced energy cut-off (30 Ry, 408 eV) and the *k*-points mesh (Γ point) were used in order to save computing time without compromising accuracy. The justification of such an approach was validated in a previous work [37].

After QMD equilibration, the geometry of the heterostructure was optimized by simultaneously relaxing the supercell basis vectors and the positions of atoms inside the supercell using the BFGS algorithm [36]. The Monkhorst-Pack (2 2 2) mesh was used [38]. The relaxation of the atomic coordinates and of the supercell was considered to be complete when atomic forces were less than 1.0 mRy/Bohr (25.7 meV/Å), stresses were smaller than 0.05 GPa, and the total energy during the structural optimization iterative process was changing by less than 0.1 mRy (1.36 meV). For the generated heterostructures, we introduced the following abbreviation: "ZT" and "HT" refers to heterostructures generated at 0 K and 1400 K, respectively. The tensile stress-strain relations

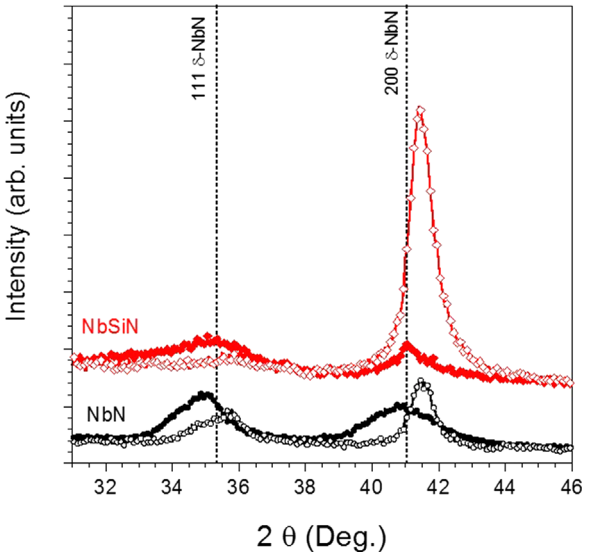

Fig. 4. XRD patterns of the NbN and Nb-Si-N films deposited at $U_B = -70$ V before (shaded circles) and after (non-shaded circles) vacuum annealing.

Table 3
Second order elastic constants C_{11}, C_{12} and C_{44} (in GPa), anisotropy factor *A*, Young modulus *E* (in GPa) and Poisson ratio ν of cubic NbN compound obtained from first-principle calculations or experimental data of the literature.

C_{11}	C_{12}	C_{44}	A	E	ν	Ref.
590	143	80	0.36	295	0.332	Calc.[a]
673	128	103	0.38	361	0.306	Calc.[b]
568	179	108	0.56	358		Calc. [55]
628	133	103	0.42	582	0.174	Calc. [56]
630	134	85	0.34	346	0.307	Calc. [57]
649	136	80	0.31			Calc. [58]
697	101	94	0.32			Calc. [59]
498	212	89	0.62			Calc. [60]
556	152	125	0.62			Expt. [61]
608	134	117	0.49			Expt. [48]

[a] Present calculations for NbN.
[b] Present calculations for $NbN_{0.75}$.

Table 4
Results of the XRD stress analysis of films deposited at −70 V and annealed at 1000 °C.

Coating	a_0 (Å)	Stress σ (GPa)
As-deposited NbN	4.401 ± 0.005	-3.2 ± 0.2
Annealed NbN	4.357 ± 0.005	1.8 ± 0.3
As-deposited Nb-Si-N	4.357 ± 0.007	-4.3 ± 0.9
Annealed Nb-Si-N	4.336 ± 0.007	-6.0 ± 0.7

were calculated by: 1) elongating the supercells along the c-axis in an incremental step, 2) fixing of the c basis vector and 3) simultaneously relaxing the a-and b-basis cell vectors and the positions of the atoms within the supercell. The stress of the heterostructures under shear strains was calculated as follows: first an incremental shear distortion was imposed, then, the basis supercell vectors orthogonal to the applied strain and the atomic coordinates were relaxed. For both tensile and shear strains the structural parameters at a previous step were used to calculate the Hellmann-Feynman stress for the next step.

To validate our computational method, we also studied the bulk properties of δ-NbN compound. The calculated lattice constant, $a_{NbN} = 4.41$ Å, was found to be close to the experimental value of 4.394 Å, and comparable to other theoretical results of 4.378–4.42 Å [39]. The elastic constants for δ-NbN_x compounds

Table 5
Chemical composition of the NbN and Nb-Si-N films (in at%).

Coatings	Nb	Si	N	O	Nb/Si	Method
NbN ($U_b = -70$ V)						
As-deposited	40.3	/	54.4	4.3	/	WDS
Vac. annealed	39.8	/	53.8	6.4	/	WDS
NbN ($U_b = -50$ V)						
As-deposited	44.5	/	55.5	N. A	/	XPS
Nb-Si-N ($U_b = -70$ V)						
As-deposited	27.4	11.9	55.7	5.0	2.3	WDS
Vac. annealed	29.6	10.2	55.2	5.0	2.9	WDS
Nb-Si-N ($U_b = -50$ V)						
As-deposited	37.0	14.8	48.2	N. A	2.5	XPS

(x=1 and x=0.75) were calculated using cubic Nb_4N_4 and Nb_4N_3 cells and the Monkhorst-Pack (8 8 8) mesh in the framework of the formalism [40]. Besides, the computational procedures were tested in simulations of similar heterostructures consisting of other materials [37,38,41,42]. The motivation for the selection of the NbN/SiN_x interfaces in the present investigation (cf. Table 1) is the fact that these types of interfaces have been reported in a number of transition metal nitrides/silicon nitrides nanocomposites [37,41–46].

3. Results and discussion

3.1. Experimental results

Fig. 1 shows the AFM surface topography of the NbN and Nb-Si-N films deposited at various U_B. One can see that the film surface roughness increases with U_B. In addition, the surface roughness in Nb-Si-N films is smaller than in NbN films, which can be due to the formation of a nanocomposite structure with smaller grain size and presence of amorphous SiN_x matrix (see below). It follows that a decrease in substrate bias U_B and an introduction of silicon promote the reduction of surface roughness.

In Fig. 2 we show the XRD patterns of the NbN and Nb-Si-N films deposited at different U_B. For the NbN film deposited at $U_B = 0$, we can observe the (111) and (200) reflexions from the cubic crystal lattice (δ-NbN, NaCl structure type, PDF No. 38-1155, cf. Fig. 2a, XRD-pattern 1). In the case of Nb-Si-N film (cf. Fig. 2a, XRD-pattern 2), we observe strong reflexions from the cubic δ-NbN phase. For both films we note the (200) predominant orientation of the growth of δ-NbN crystallites. Asymmetry of δ-NbN XRD lines towards large angles indicates the existence of so-called packing defects that are usually observed for highly strained films.

For NbN films, an application of substrate bias of −40 V caused the enhancement of the (111) reflexion (cf. Fig. 2b, spectrum 1). However, in the case of Nb-Si-N films, an application of substrate bias did not influence strongly the XRD pattern: the clear preferential orientation of the crystallites along the [100] axis, perpendicular to the plane of growth, was preserved. We should also note that, for this film, weak reflexions from δ-NbN at $2\theta = 70°$ and 90° were detected.

A further increase in U_B up to −70 V during the deposition of NbN films resulted in significant XRD line broadening without changing preferential orientation (cf. Fig. 2c, XRD-pattern 1). A remarkable change in the XRD pattern of the Nb-Si-N film occurs after deposition at $U_B = -70$ V. In particular, the strong δ-NbN(111) reflexion and broad peak in the range of $2\theta = 30–38°$ appear (Fig. 2c, XRD-pattern 2). The latter feature can be explained by

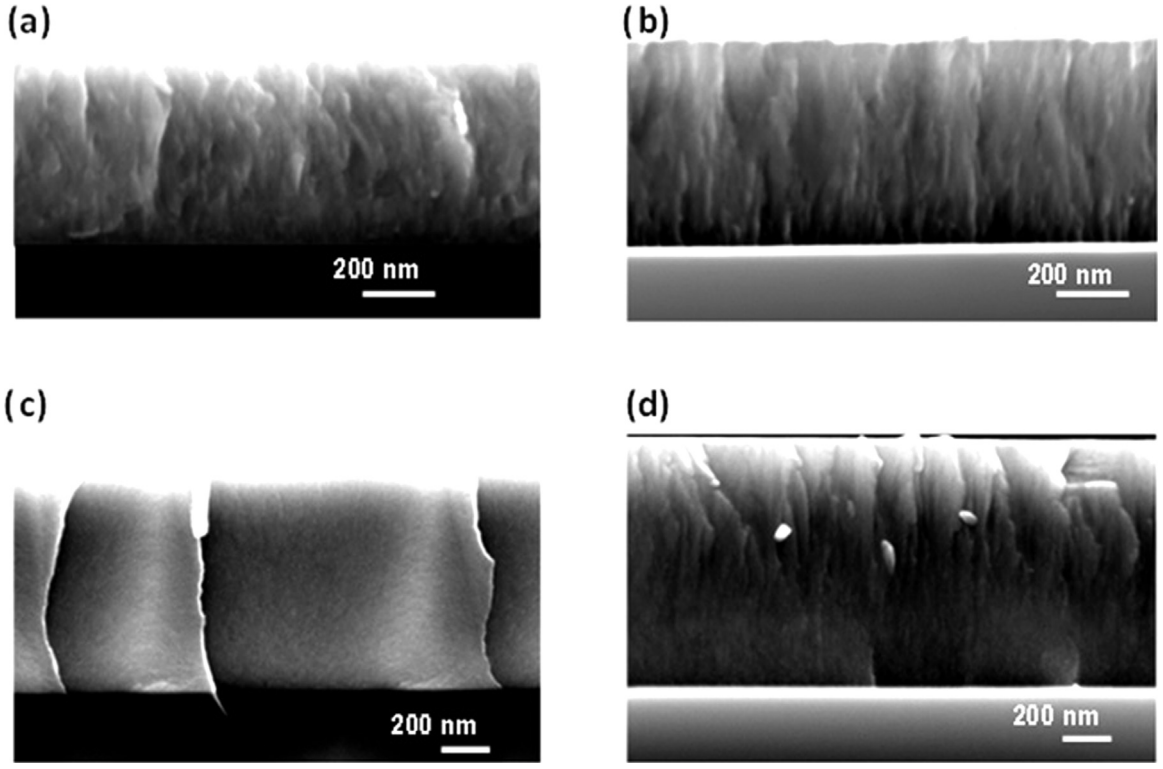

Fig. 5. Cross-sectional SEM images of NbN films (a-b) and Nb-Si-N films (c-d) deposited at $U_B = -70$ V, in their as-deposited (a, c) and vacuum annealed (b, d) states.

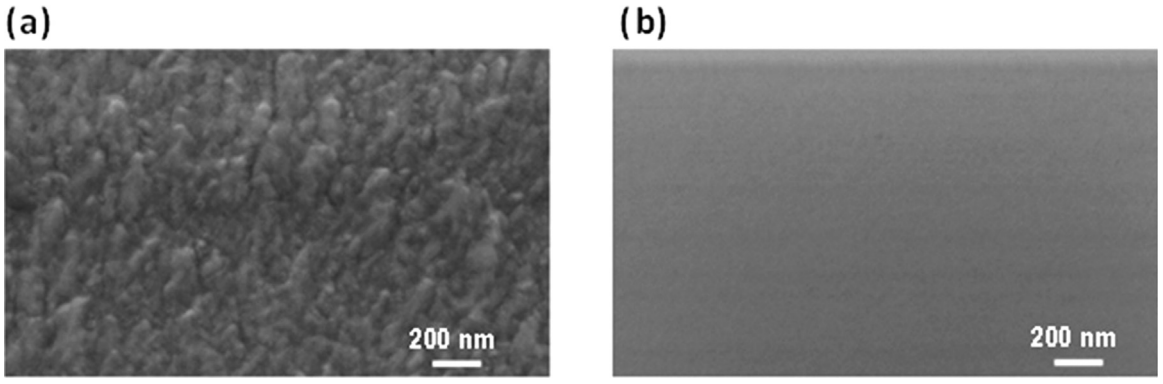

Fig. 6. Plan-view SEM images of the surface of the NbN (a) and Nb-Si-N films deposited at $U_B = -70$ V.

superposition of scattered intensity from crystalline and amorphous phases related to silicon nitride. We assumed, that halo peak in the angle range $2\theta = 30–38^\circ$ belongs to amorphous-like phase of silicon nitride on the basis of the works [47], where the authors showed the transition of such state into Si_3N_4 crystallites during high-temperature annealing. It is possible if on the stage of short-range ordering in the amorphous-like state coupled regions of Si and N atoms ((a-SiN)) are created as a prototype of further crystallization into the Si_3N_4 phase. The thermodynamic factor, which determined primary bond between Si and N atoms in amorphous-like state, is a large energy gain in the formation of silicon nitride. We note that such broadening of the XRD lines and the formation of diffuse scattering from amorphous-like state are typical features of the films deposited at large bias potentials. It is well known that large bias voltages promote a refinement of grains and an enhancement of biaxial stress. In our case, an increase in U_B also alters the preferred orientation of Nb-Si-N films.

We analyzed the structure of the deposited NbN and Nb-Si-N films using a fitting procedure of XRD line profiles by Cauchy functions. The main results of the structural analysis are presented in Table 2. One can see from Table 2 that incorporation of Si decreases microstrain of the crystallites and their average size.

It is seen from the Table 2, that the structure of the films deposited at -40 V and -70 V is significantly influenced by the annealing, as revealed by the strong increase of the average crystallites size and decrease of microstrain by a factor two. However, the grounded Nb-Si-N films were found to be thermally stable after annealing. They also exhibited a low microstrain level (0.5%), even in their as-deposited state. This can be explained by the lower concentration of ion bombardment-induced defects.

Fig. 3 shows the evolution of the lattice parameter of NbN crystallites measured from (200) interplanar spacings as a function of $sin^2 \psi$ for NbN and Nb-Si-N films deposited at $U_b = -70$ V. A linear variation is observed for the NbN film, while deviation from linearity is noticed in the presence of Si atoms. This can reflect the presence of stress gradients along the film depth or a more complex stress state due to the presence of neighboring interacting crystallites with hexagonal structure. The deviation from linear dependence may be also due to the change of the nature of the interatomic bonding from more ionic for NbN to more covalent for

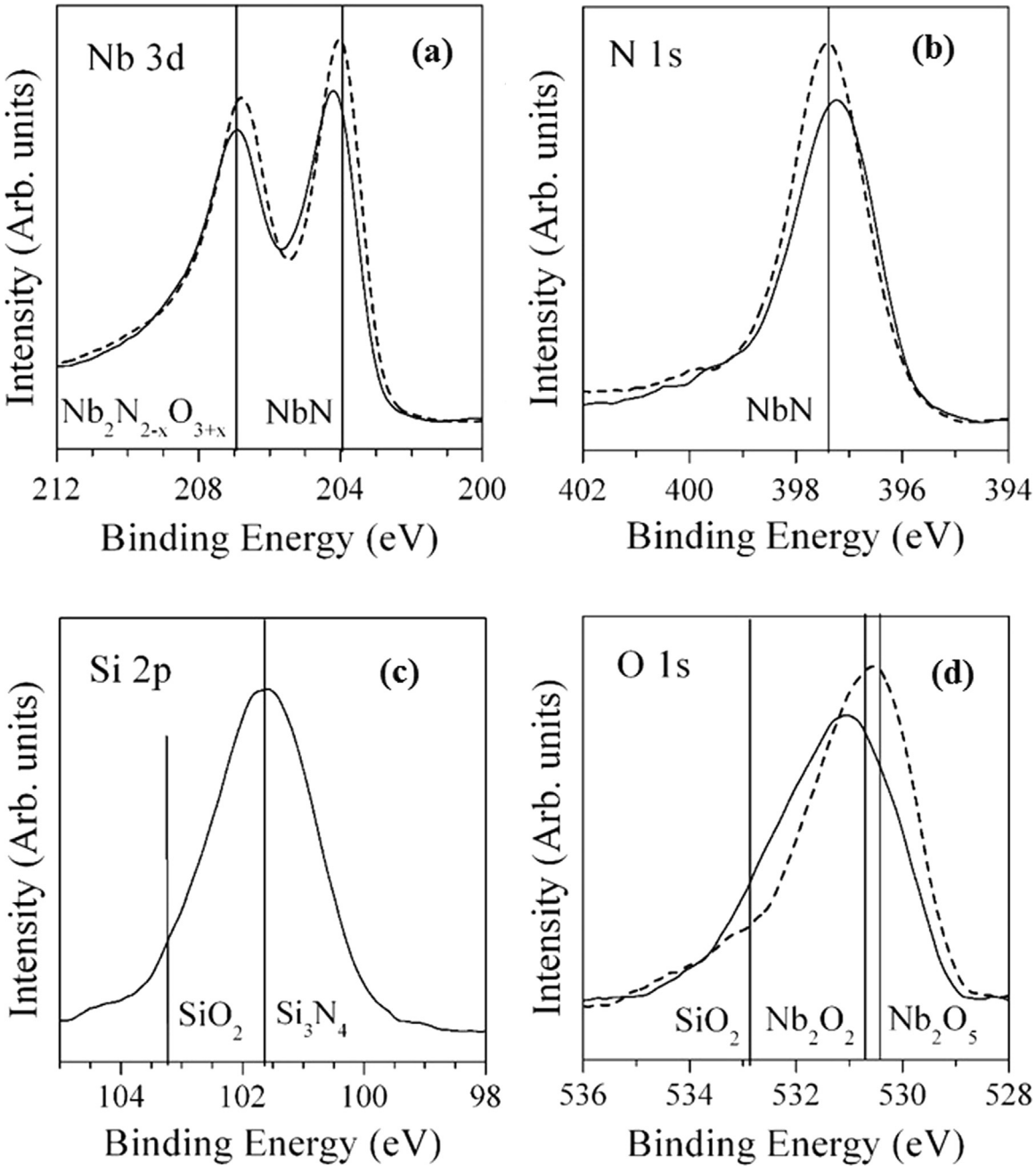

Fig. 7. Core-level XPS spectra for NbN (solid line) and Nb-Si-N (dashed line) ($U_B = -50$ V): Nb 3d states (a) N 1 s states (b), Si 2p states (c) and O 1 s states (d).

SiN. However, it can be seen that the presence of Si decreases the lattice parameter of NbN crystals. This decrease can be explained either by appearance of vacancies in nitrogen sublattice (i.e. formation of non-stoichiometric films) or by partial substitution of Nb atoms by Si ones in the crystal lattice. The as-deposited films are under a compressive stress state, as evidenced from the negative slope of the $sin^2\psi$ plots. After annealing at 1000 °C, the lattice parameter of both films is found to be smaller. For the NbN film, a tensile stress state is finally reached, while the stress is still compressive for the Nb-Si-N nanocomposite film, despite a clear improvement of film crystallinity (see Fig. 4), associated with a decrease of microstrain and increase of average size of crystallites.

The stress analysis was performed assuming a macroscopically (elastically) isotropic specimen, subjected to a rotationally symmetric in-plane biaxial stress state, $\sigma_1 = \sigma_2 = \sigma$. For a cubic material, the strain-stress relation is given by

$$\varepsilon_{hkl} = \frac{a_{hkl} - a_0}{a_0} = \left(2S_1^{hkl} + \frac{1}{2}S_2^{hkl} Sin^2\psi\right)\sigma,$$

where S_1^{hkl} and S_2^{hkl} are the so-called X-ray elastic constants (XECs) for the *{hkl}* reflections employed in the diffraction measurements, and a_0 is the stress-free lattice parameter. The XECs differ from the mechanical elastic constants, $S_1^{mech} = -\frac{\nu}{E}$ and $S_2^{mech} = \frac{2(1+\nu)}{E}$ usually employed to describe the behavior of isotropic polycrystalline aggregates, where E is the Young modulus and ν the Poisson ratio. NbN is characterized by a significant elastic anisotropy, as the anisotropy factor $A = 2C_{44}/(C_{11} - C_{12})$ is much lower than 1, it varies between 0.31 and 0.62 depending on reported values of the literature (cf. Table 3). It is seen that our results for NbN and $NbN_{0.75}$ agree well with the experimental and theoretical data of other authors. The presence of nitrogen vacancies leads to an increase of the Young modulus and anisotropy factor and to a lowering of the Poisson ratio, which points to the strengthening of

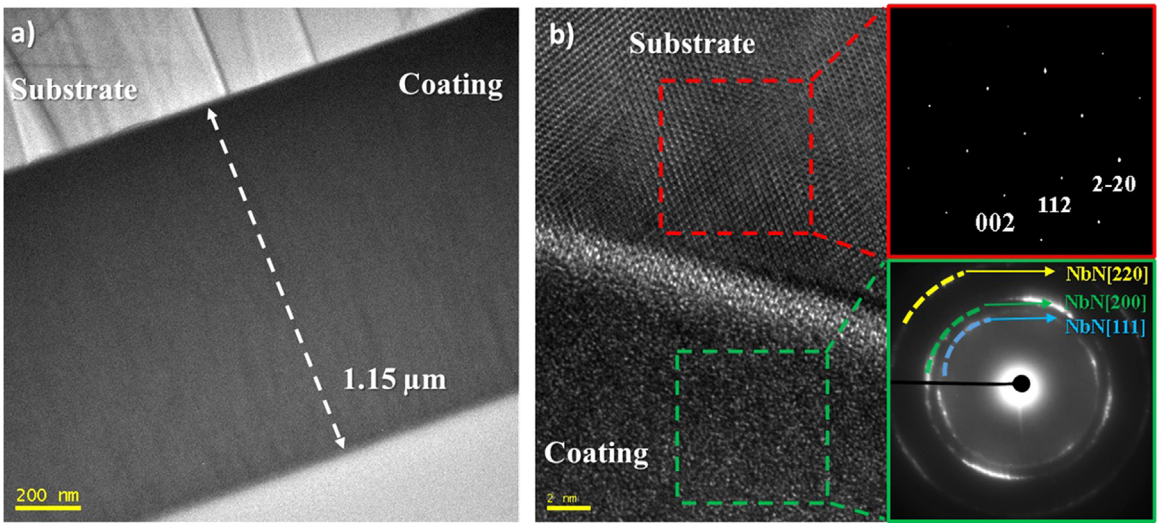

Fig. 8. Cross section images of the Nb-Si-N film deposited at $U_B = -70$ V (a) total thickness of the film (b) high magnification of the interface with SAED diffraction insets. (Zone axis [110]).

N-deficient niobium nitride. In the present analysis, the XECs were calculated for the {200} reflection using the experimental data reported by Chen and co-workers [48] and assuming a Reuss model (i.e. equal stress state for all crystallites; see Appendix A [31] for the detailed expressions). The results of stress analysis are reported in Table 4.

One can see that compressive stresses with magnitude of 3–4 GPa are obtained in the as-deposited films. The bombardment of the growing film with ions accelerated across the substrate sheath – they acquire an energy of $(U_p - U_B)$, where U_p is the plasma potential – is at the origin of defect incorporation into the NbN crystallites, a phenomenon often referred as atomic peening. The stress-free lattice parameter of NbN film is found to be slightly expanded compared to the bulk value (4.394 Å), suggesting the presence of defects acting as misfitting particles associated with hydrostatic stress component [32,49]. During vacuum annealing at 1000 °C, there exist sufficient atomic mobility to ensure annihilation of growth-induced defects and grain boundary migration, resulting in grain growth. The next result is the development of tensile stress with magnitude of 1.8 GPa. The fact that the stress-free lattice parameter becomes lower after annealing than the bulk value of NbN suggests alteration of the chemical composition of the coating. WDS analyses reveal a slight incorporation of oxygen atoms (+1.5 at%) after annealing together with a loss of nitrogen atoms (−1 at%). A similar behavior is observed for the Nb-Si-N nanocomposite film. In this latter case, the oxygen and nitrogen contents were found to remain unchanged (see Table 5), while the Nb/Si ratio changed from 2.3 to 2.9 after annealing.

Cross-sectional SEM images are presented in Fig. 5 for NbN and Nb-Si-N films deposited at $U_B = -70$ V. No clear columnar structure could be seen on the as-deposited fractured samples and the films appear to have a very dense microstructure. In particular, for the Nb-Si-N film (Fig. 5c), a fine grained globular morphology is discernible at higher magnification. This is in line with XRD results of Fig. 2c, where a significant line broadening was observed at $U_B = -70$ V. After vacuum annealing (Fig. 5b-d, one can notice that film integrity is preserved, although delamination at the coating/substrate interface can occur locally. Some columns are visible in the upper part of the annealed Nb-Si-N film (Fig. 5d), which can be ascribed to grain growth or recrystallization based on XRD patterns of Fig. 4. No oxidized layer could be observed in the annealed coatings, showing their good thermal stability, in agreement with WDS analyses on annealed films (see Table 5). Fig. 6b shows the SEM image of the surface of the Nb-Si-N film deposited at $U_B = -70$ V, comparatively to the NbN film deposited under the same deposition conditions (Fig. 6a). The featureless surface morphology is consistent with the AFM observation of Fig. 1 for the high-biased Nb-Si-N film and testifies the high degree of compactness of this film.

To identify the structure of the amorphous tissue we measured the core-level XPS spectra of the NbN and Nb-Si-N films deposited at −50 V. The measured XPS spectra of the as-deposited film are presented in Fig. 7. It is known that a native oxide grows on Nb compounds when exposed to air [25], and the peaks at 204.07 eV and 206.88 eV can be assigned to Nb 3d states in NbN (203.97 eV [27]) and $Nb_2N_{2-x}O_{3+x}$ (207.0 eV [50]), respectively. For NbN films, the peak at 397.4 eV in the N 1 s spectrum is determined by Nb-N bonds (397.4 eV [25]), whereas for Nb-Si-N films, this peak is shifted to 397.2 eV. We suppose that the asymmetry of the N 1 s peak can be caused by the Si-N bonds in Si_3N_4 (397.8 eV [51]). XPS measurements of the Si 2p spectrum provide further information on the Si bonding in the Nb-Si-N films. The peak at a binding energy of 101.7 eV is assigned to Si in Si_3N_4 (101.7 eV [51]), and a shoulder at 103.3 eV is supposed to be due to the Si–O bonds in SiO_2 (103.5 eV [51]). Based on these findings, one can suppose that the amorphous matrix in Nb-Si-N films is close to the amorphous Si_3N_4 phase (a-Si_3N_4) with a small admixture of oxygen. We also note that the O 1 s spectra of the NbN and Nb-Si-N films are centered around 530.5 eV and 531.0 eV, respectively, and can be attributed to the Nb–O bonds in Nb_2O_5 (530.4 eV) and Nb_2O_2 (530.7 eV [51]), respectively. In the case of Nb-Si-N films, the Si–O bonds in SiO_2 can form the wide tail around 532.9 eV [51] (see Fig. 7d).

Using the XPS data, we estimated the niobium, nitrogen and silicon contents (C_{Nb}, C_N and C_{Si}, respectively) in NbN and Nb-Si-N films. It was found that $C_{Nb} = 44.5$ at%, $C_N = 55.5$ at% for NbN films and $C_{Nb} = 37.0$ at%, $C_N = 48.2$ at% and $C_{Si} = 14.8$ at% for Nb-Si-N films. These values are consistent with those obtained from WDS (see Table 5). One can see also that the XPS procedure slightly overestimates the silicon content in the films as compared to that determined from WDS measurements.

Comparison of the results presented in Figs. 1–7 enables us to establish the structure of the NbN and Nb-Si-N films. The NbN films are nanostructured, and the Nb-Si-N films have a nanocomposite structure, and represent an aggregation of δ-NbN_x nanocrystallites embedded into the amorphous Si_3N_4 tissue (nc-δ-NbN_x/a-Si_3N_4). The low-biased Nb-Si-N films are textured with the preferable (200) grain orientation.

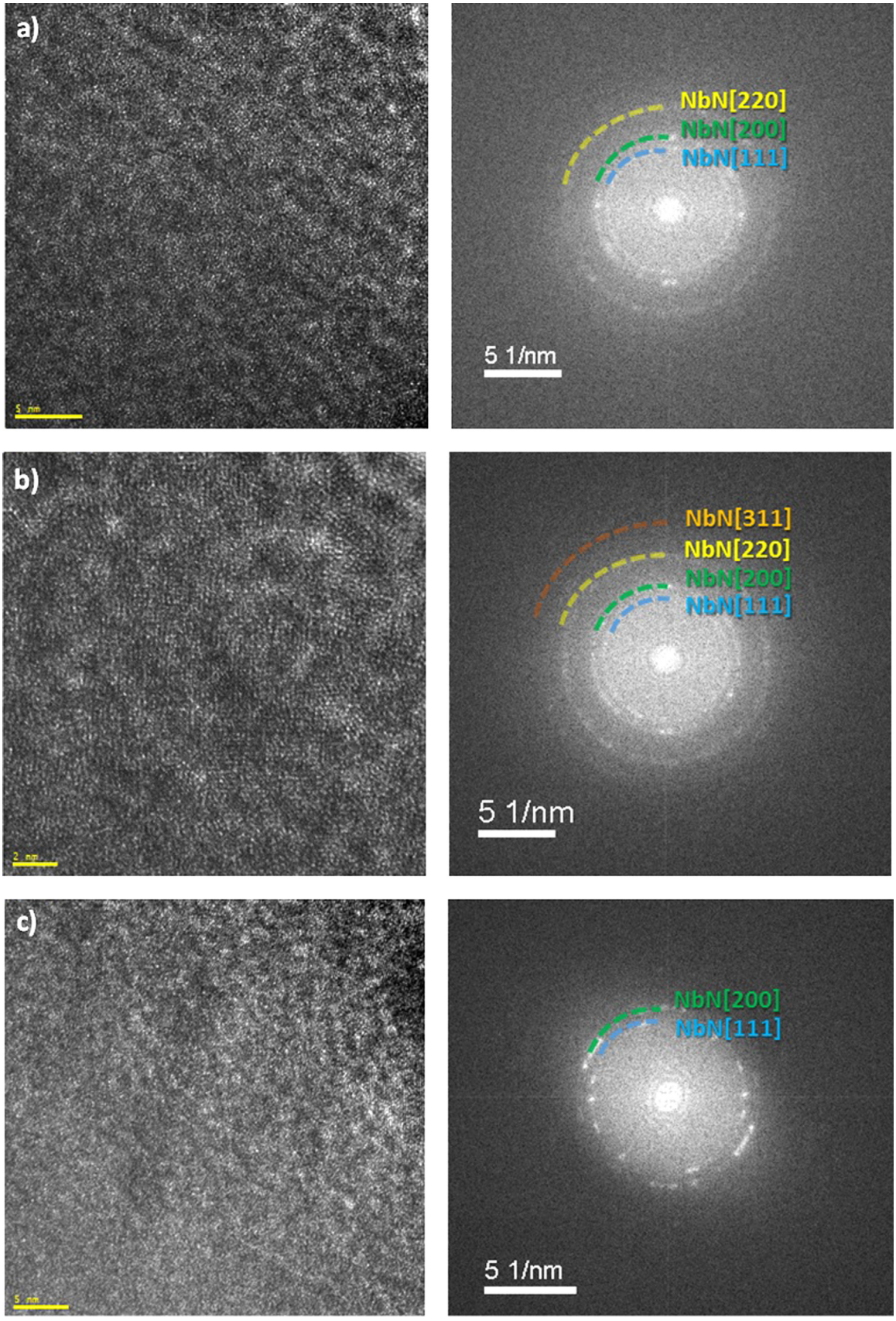

Fig. 9. HR-TEM micrographs and FFT images of Nb-Si-N thin film deposited at $U_B = -70$ V. Images were collected in regions close to the interface a), in the middle of the coating b), and near the surface c).

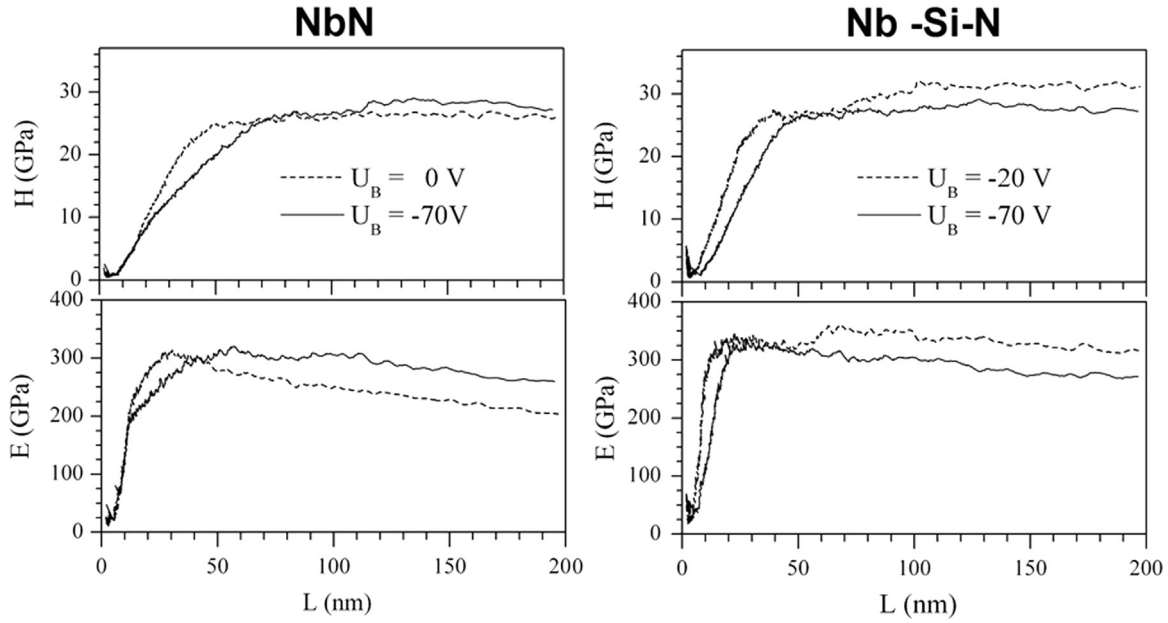

Fig. 10. Dependences of the nanohardness (H) and elastic modulus (E) on nanoindenter penetration depth (L) for NbN and Nb-Si-N films deposited at different substrate biases U_B. The H(L) and E(L) curves for the films deposited at other substrate biases fall within the corresponding curves marked as solid and dashed lines.

A cross-sectional TEM image is presented in Fig. 8a for the Nb-Si-N coating deposited at $U_B = -70$ V. The total thickness is 1.15 μm. No visible grain boundaries could be revealed at this lower magnification. EDS mapping confirmed the homogeneous distribution of the Nb and Si elements over the entire depth of the coating. A sharp interface, where the crystalline Si substrate contrasts with the nanocomposite nature of the coating, is shown in Fig. 8b. A brighter contrast is visible at the coating/Si interface, related to native oxide of Si substrate and/or possible mixing region. The nanocomposite structure is evidenced by the presence of diffuse rings with weak intense spots in the SAED pattern shown in Fig. 8b.

Further analysis focusing on different sections of the coating are shown in Fig. 9. The small crystalline regions are visualized with the help of the Fast Fourier Transform (FFT) which shows some diffuse rings with well localized spots, confirming the nanocrystalline/amorphous structure of the sample, similar to one observed in NbC nanocomposite films [52]. The FFT image shows well defined rings attributed to [111], [200], [220] and [311] of the cubic δ-NbN structure. The lattice constant is determined as $a = 4.328 \pm 0.007$, this value shows a lattice reduction from the δ-NbN bulk value, accounting for the incorporation of Si atoms in the NbN unit cell and/or presence of nitrogen vacancies, values that are consistent with the XRD data presented in Figs. 2 and 4. Moreover, the crystal size can be estimated using the FFT filtered imaged, where nanocrystallites of $3(\pm 1)$ nm are observed. EDS analysis confirms the homogeneous distribution of Nb and Si in the coating with 2.2 times more Nb than Si in the sample, values in agreement with the XPS data shown in Fig. 7 (see also Table 5).

The dependence of nanohardness (H) and elastic modulus (E) on indenter penetration depth (L) of the deposited films are presented in Fig. 10. It is seen that at larger indentation depths ($L > 100$ nm), the nanohardness practically does not depend on L and is therefore representative of the film only. The elastic modulus is maximum at $L = 50$ nm and then slightly decreases at higher L, due to the influence of the softer silicon substrate. In Fig. 10 we present the curves that correspond to the maximum and minimum values of H and E. We see that the mechanical characteristics are weakly dependent on substrate bias. An increase of U_B leads to increasing H and E in NbN films, whereas for Nb-Si-N films these characteristics decrease with increasing U_B. We will try to account for this fact below using theoretical findings. It is seen that the films with best mechanical properties correspond to H~28 GPa and E~320 GPa (NbN) and H~32 GPa and E~340 GPa (Nb-Si-N).

We found recrystallization of the coatings after high-temperature annealing (1000 °C). It was accompanied by the formation of preferred orientation of crystallites with the plane (100), which is parallel to the surface of growth that corresponds to the minimum of surface energy. In addition, we found relaxation of compressive stresses and their transition to tensile stresses during high-temperature annealing (1000 °C) of NbN films on Si substrates. Doping of the coatings by Si during deposition and formation of two-phase state (δ-NbN and SiN_x phases) prevents relaxation of the compressive stresses during annealing. Distribution profile of the stress state is heterogeneous.

3.2. Theoretical results and the interpretation of experimental data

In Fig. 11 we show the atomic configurations of the HT heterostructures under consideration. The geometry optimization of the initial δ-Si_3N_4 heterostructure at 0 K (not shown here) preserved the heteroepitaxial arrangement for the interface in a similar way as described for the TiN(001)/$Si_{0.75}N$ heterostructure [37]. The geometry of the (001) interface was preserved, but the nitrogen atoms above and below the interface were slightly shifted toward this interface. However, at 1400 °K, the (001) interfacial structure significantly changed (cf. Fig. 11a). There is an almost symmetrical, "down" and "up" shift of the N atoms in the layer just above and below the interfacial layer, an almost random shift of the Si atoms within the interfacial plane, and breaking of about half of the Si-N bonds. This leads to the formation of distorted over-coordinated Si_3N_4–like units that are represented by the SiN_4 and SiN_5 units. One can see from Fig. 11a that, along with the new Si_3N_4–like units, some of the original six-fold coordinated SiN_6 units are still present albeit distorted. More information about this interface can be found elsewhere [30].

The hexagonal δ-SiN, δ-coherent SiN and ε-Si_2N_3 heterostructures shown in Fig. 11c, d and e, respectively, are found to be stable and weakly dependent on temperature in the range of 0–1400 K. The interfaces in the HT δ-Si_2N_3 and ε-SiN heterostructures are slightly disordered (cf. Fig. 11b and f) compared to

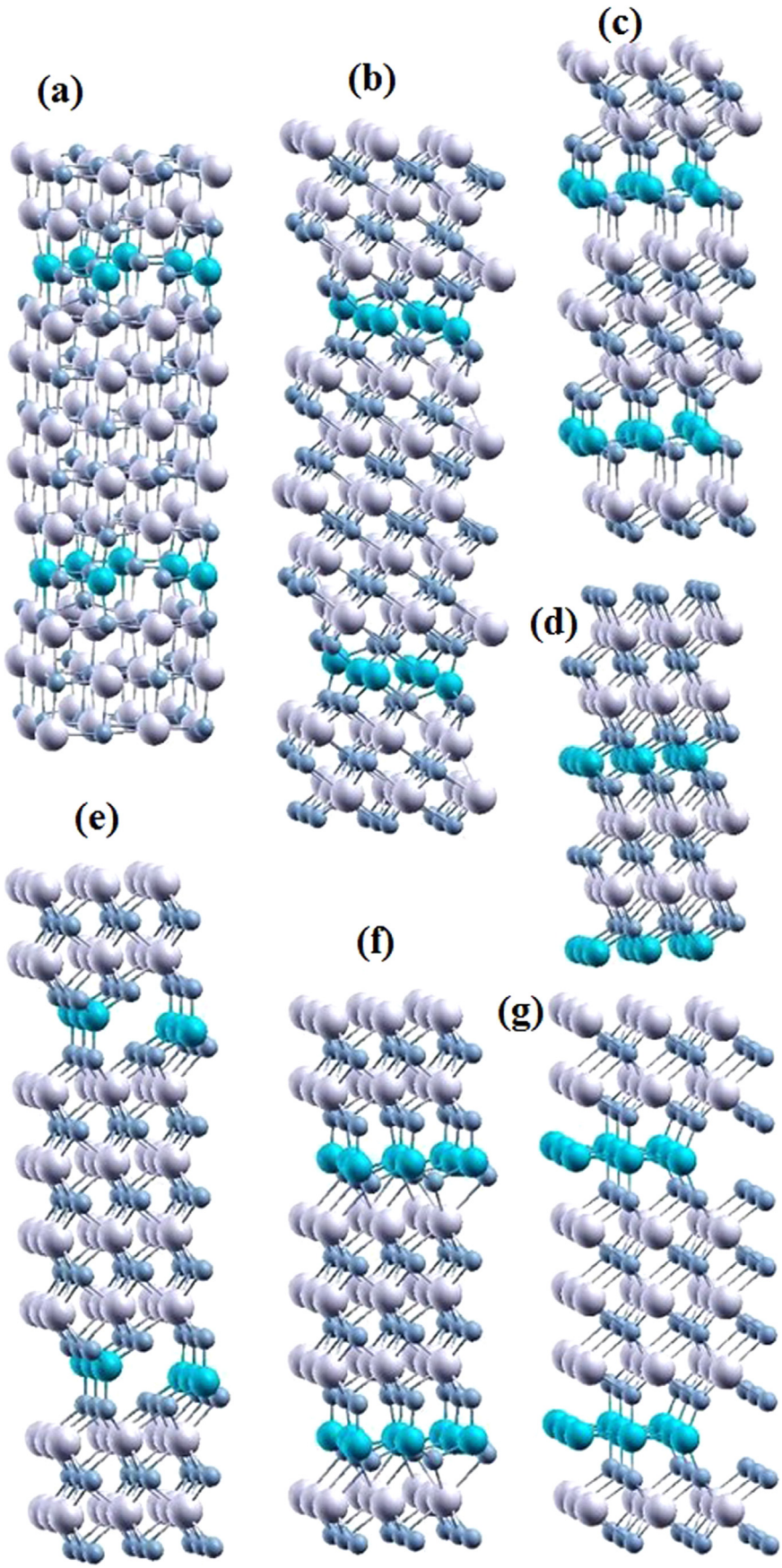

Fig. 11. Atomic configurations of the HT heterostructures: δ-Si_3N_4 (a), δ-Si_2N_3 (b), δ-SiN (c), δ-coherent SiN (d), ε-Si_2N_3 (e), ε-SiN (f), ε-coherent SiN (g). The supercells are translated in the z-direction. The large, middle and small circles are the niobium, silicon and nitrogen atoms, respectively. The bond length cutoffs are: 2.3 Å (Si-N) and 2.6 Å (Nb-N).

those in the initial heterostructures. The four-fold coordination of the silicon atoms is preserved. The total energy of these heterostructures increases insignificantly compared to that of the initial relaxed heterostructures (by 0.003 eV/atom). The interface in the ε-coherent SiN heterostructure changed during the initial relaxation, and its temperature modification was insignificant (cf. Fig. 11g). The Si atoms on this interface are surrounded by four silicon and two nitrogen atoms, whereas the initial heterostructure consisted only of SiN_6 units.

The calculated stress-strain dependencies, $\sigma(\varepsilon)$, of the bulk NbN phase and the various HT NbN/SiN_x heterostructures are shown in Figs. 12 and 13. The ideal tensile strength, σ_T, corresponds to the maximum stress before failure. Values of σ_T derived from the stress-strain relations are summarized in Table 1. It is seen that the formation of the SiN_x interfaces in NbN leads to a reduction of ideal tensile strength. This means that interface formation does not result in a strengthening of the nanocomposites based on NbN/SiN_x from a chemical bonding perspective, as was shown for TiN/SiN_x heterostructures [53]. Due to symmetry and the specific electronic structure of different phases of NbN [54] the values of σ_T for the hexagonal structures are higher than for the cubic ones, for which reason the mechanical characteristics for ε-NbN films should be higher than for δ-NbN ones, in agreement with experiments [14,15].

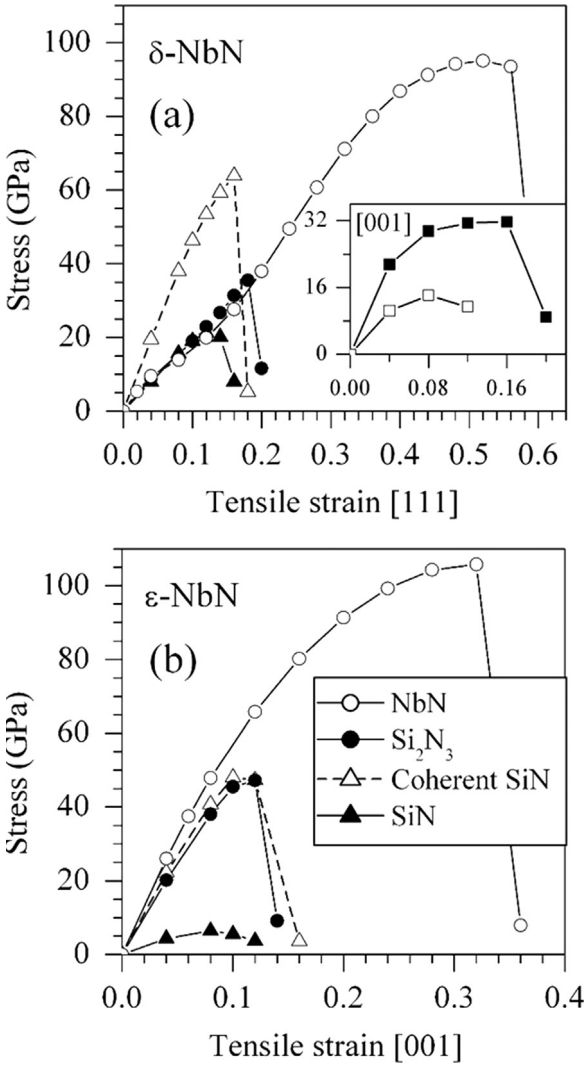

Fig. 12. Calculated tensile stress-strain curves for the bulk NbN and HT heterostructures based on δ-NbN (a) and ε-NbN (b); see notations in Table 1. Tensile strains were in the (111) direction (δ-NbN–based heterostructures) and the (001) direction (ε-NbN–based heterostructures). In the insert: the tensile stress-strain curves for δ-NbN(001) (full squares) and δ-Si_3N_4 (open squares) structures.

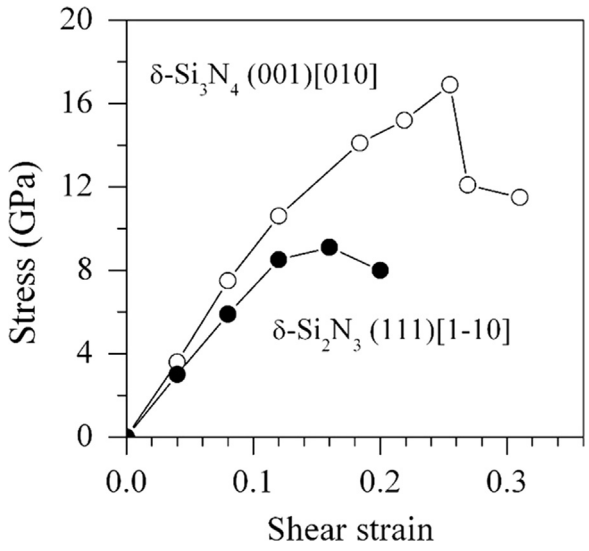

Fig. 13. Calculated shear stress-strain curves for the HT heterostructures based on δ-NbN (cf. Table 1).

Several important features can be gained from these calculations to understand experimental findings. It is well known that the elastic modulus is determined by the slope of the stress-strain curve at small tensile strains: the higher the slope, the larger the elastic modulus. A careful analysis of the slopes of the $\sigma(\varepsilon)$ curves shown in Fig. 12 indicates that the Young moduli for the δ-NbN(001)/Si_3N_4 and δ-NbN(111)/Si_3N_4-like Si_2N_3 heterostructures should approximate 263 GPa and 223 GPa, respectively. It follows that a decrease in the elastic modulus of the deposited Nb-Si-N films with increasing substrate bias can be assigned to an enhancement of the δ-NbN(111) texture. The ideal tensile strength for the heterostructures with the coherent interfaces and the Si_2N_3 interfaces are highest (cf. Table 1, Fig. 12). We calculated the formation energy of a single Si vacancy (E_V) for the heterostructures with the SiN interfaces. The values of E_V were −2.943, −0.590 and 2.233 eV/atom for the δ-NbN(001)/coherent SiN, δ-NbN(111)/coherent SiN and ε-NbN(001)/coherent SiN heterostructures, respectively. It follows that, for the δ-NbN–based heterostructures, the coherent SiN interfaces are unstable with respect to a formation of Si vacancies, and the more realistic interfaces in δ-NbN/SiN_x nanocomposites will be Si_3N_4–like interfaces, in agreement with our experimental results. On the contrary, the stoichiometric coherent SiN interface in the ε-NbN(001)/SiN heterostructure is quite stable with respect to the formation of Si vacancies. This means that the ε-NbN–based nanocomposites with the coherent SiN interface will be stable at nanoscale and should exhibit the best mechanical properties. Nevertheless, based on our theoretical results, we note that the formation of both the stoichiometric and substoichiometric interfacial silicon nitride layers in ε-NbN and δ-NbN destabilizes niobium nitrides. Therefore, the observed strength enhancement in the NbN/Si_3N_4 nanocomposite films should be ascribed mostly to the interfaces that play the role of barriers inhibiting dislocation motion.

Let us estimate an effect of the interfaces on the hardness of the deposited Nb-Si-N films. It is assumed that an “intrinsic” hardness of a material correlates to its ideal shear strength for a weakest shear system. We calculated the shear stress-strain relations for the two δ-Si_3N_4 and δ-Si_2N_3 heterostructures, as representative of interfaces found experimentally for (001) and (111) oriented films (cf. Fig. 2). In Fig. 13, the shear stress-strain relations for the δ-Si_3N_4 and δ-Si_2N_3 heterostructures are presented. We see that

the ideal shear strength for the δ-NbN(001)-based heterostructure is higher compared to that for the δ-NbN(111)-based one, which can account for the lowering of the hardness of the films when forming preferential NbN(111) crystallites (cf. Figs. 2 and 10).

4. Conclusions

NbN and Nb-Si-N films were deposited on silicon wafers by magnetron sputtering at various substrate biases varying between 0 and −70 V. The comparative investigation of the structural and mechanical properties of the deposited films was carried out. AFM and SEM investigations show that a decrease in U_B and an introduction of silicon promote the reduction of the surface roughness of the films. Based on XRD, XPS and TEM observations the structure of the deposited films was established: the NbN films were nanostructured, and the Nb-Si-N films had a nanocomposite nc-δ-NbN_x/a-Si_3N_4 structure with a small admixture of oxygen in the amorphous matrix. The NbN films deposited under negative bias consist of δ-NbN crystallites. In contrast to the NbN films, the low-biased Nb-Si-N films ($U_B < -70$ V) are textured with the preferential (200) orientation. The Nb-Si-N films exhibit hardness of H~32 GPa which is higher than that of the NbN films (H~28 GPa) mainly due to the formation of the nanocomposite nc-δ-NbN_x/a-Si_3N_4 structure. For Nb-Si-N films, an application of higher bias potential resulted in a depletion of the light atoms.

It was shown that the structure of the Nb-Si-N film deposited at −70 V was strongly influenced by annealing at 1000 °C. The average size of crystallites increased from 9.1 nm to 150 nm, and microstrain changed from 0.6% to 0.3%.

The results of first principles molecular dynamics simulations of the NbN/SiN_x heterostructures at 0 K and 1400 K show that the high-temperature interface in the cubic δ-NbN(001)/Si_3N_4 heterostructure consists of distorted over-coordinated Si_3N_4–like units, as well as the original six-fold coordinated δ-SiN_6 units. The hexagonal heterostructures are weakly dependent on temperature. Calculations of the stress-strain curves show that the values of ideal tensile strength for the heterostructures with the coherent SiN interfaces and the Si_3N_4-like Si_2N_3 interfaces are the highest. The ideal shear strength of the δ-NbN(001)-based heterostructure was found to be higher compared to that of the δ-NbN(111)-based one. These finding can be considered as one of plausible explanations for lowering the hardness of the Nb-Si-N films when forming NbN(111) crystallites.

Acknowledgments

This work was done under the aegis of scientific-technical collaboration program between Sumy State University (Sumy, Ukraine) and University of Poitiers (Institut P', University of Poitiers, Poitiers, France), and Ukrainian complex state budget programs "Creation of basis of superhard nanostructure coatings fabrication with high physical and mechanical properties" (registration number 0112U001382) and "Physical principles of plasma technologies for complex treatment of multicomponent materials and coatings" (registration number 0113U000137c). In addition, this work was partially supported by STCU Contract No. 5964 and by financial support from the National Centre for Research and Development (Contract number PBS1/A9/13/2012). The authors are grateful to Prof. Stan Veprek for his participation in the discussion of the results, as well to Dr. I. I. Timofejeva and Dr. S. N. Dub for XRD investigations and nanoindentation of the films, respectively, to A.V. Pshyk for the FIB preparation of the coatings. The presented results were partially reported on the International conferences NAP-2014 and NAP-2015.

References

[1] S.A. Barnett, A. Madan, I. Kim, K. Martin, Stability of nanometer-thick layers in hard coatings, MRS Bull. 28 (2003) 169–172, http://dx.doi.org/10.1557/mrs2003.57.
[2] Y. Gotoh, M. Nagao, T. Ura, H. Tsuji, J. Ishikawa, Ion beam assisted deposition of niobium nitride thin films for vacuum microelectronics devices, Nucl. Instrum. Methods Phys. Res. Sect. B Beam Interact. Mater. At. 148 (1999) 925–929.
[3] Z. Wang, H. Terai, A. Kawakami, Y. Uzawa, Interface and tunneling barrier heights of NbN/AlN/NbN tunnel junctions, Appl. Phys. Lett. 75 (1999) 701, http://dx.doi.org/10.1063/1.124487.
[4] P. Zhukowski, J. Sidorenko, T. Kołtunowicz, J. Fedotova, A. Larkin, Magnetic properties of nanocomposites (CoFeZr)x(Al2O3)1 − x, Prz. Elektrotechniczny 86 (2010) 296–298 ⟨http://yadda.icm.edu.pl/yadda/element/bwmeta1.element.baztech-article-BPOC-0057–0091?q=bwmeta1.element.baztech-volume-0033–2097-przeglad_elektrotechniczny-2010-r__86_nr_7;89&qt=CHILDREN-STATELESS⟩.
[5] I. Svito, J.A. Fedotova, M. Milosavljević, P. Zhukowski, T.N. Koltunowicz, A. Saad, et al., Influence of sputtering atmosphere on hopping conductance in granular nanocomposite (FeCoZr)x(Al2O3)1 − x films, J. Alloy. Compd. 615 (2014) S344–S347, http://dx.doi.org/10.1016/j.jallcom.2013.12.061.
[6] I.A. Svito, A.K. Fedotov, A. Saad, M. Milosavljević, J.A. Fedotova, T. N. Kołtunowicz, et al., Low-temperature DC carrier transport in $(Fe_{0.45}Co_{0.45}Zr_{0.10})x(Al_2O_3)1-x$ nanocomposites manufactured by sputtering in pure ar gas atmosphere, Adv. Condens. Matter Phys. 2015 (2015) 1–5, http://dx.doi.org/10.1155/2015/320187.
[7] S. Veprek, Recent search for new superhard materials: Go nano! J. Vac. Sci. Technol. A Vac. Surf. Film 31 (2013) 050822, http://dx.doi.org/10.1116/1.4818590.
[8] R.A. Andrievski, I.A. Anisimova, V.P. Anisimov, Structure and microhardness of TiN compositional and alloyed films, Thin Solid Films 205 (1991) 171–175, http://dx.doi.org/10.1016/0040-6090(91)90299-D.
[9] P.J. Martin, A. Bendavid, The filtered arc process and materials deposition, Surf. Coat. Technol. 142–144 (2001) 7–10, http://dx.doi.org/10.1016/S0257-8972(01)01135-5.
[10] A. Bendavid, P. Martin, T. Kinder, E. Preston, The deposition of NbN and NbC thin films by filtered vacuum cathodic arc deposition, Surf. Coat. Technol. 163–164 (2003) 347–352, http://dx.doi.org/10.1016/S0257-8972(02)00623-0.
[11] V.N. Zhitomirsky, I. Grimberg, L. Rapoport, N.A. Travitzky, R.L. Boxman, S. Goldsmith, et al., Structure and mechanical properties of vacuum arc-deposited NbN coatings, Thin Solid Films 326 (1998) 134–142.
[12] R.L. Boxman, V.N. Zhitomirsky, I. Grimberg, L. Rapoport, S. Goldsmith, B. Z. Weiss, Structure and hardness of vacuum arc deposited multi-component nitride coatings of Ti, Zr, and Nb, Surf. Coat. Technol. 125 (2000) 257–262, http://dx.doi.org/10.1016/S0257-8972(99)00570-8.
[13] V.N. Zhitomirsky, Structure and properties of cathodic vacuum arc deposited NbN and NbN-Based multi-component and multi-layer coatings, Surf. Coat. Technol. 201 (2007) 6122–6130, http://dx.doi.org/10.1016/j.surfcoat.2006.08.125.
[14] M. Benkahoul, E. Martinez, A. Karimi, R. Sanjinés, F. Lévy, Structural and mechanical properties of sputtered cubic and hexagonal NbNx thin films, Surf. Coat. Technol. 180–181 (2004) 178–183, http://dx.doi.org/10.1016/j.surfcoat.2003.10.040.
[15] G.A. Fontalvo, V. Terziyska, C. Mitterer, High-temperature tribological behaviour of sputtered NbNx thin films, Surf. Coat. Technol. 202 (2007) 1017–1022, http://dx.doi.org/10.1016/j.surfcoat.2007.07.043.
[16] M. Wen, C.Q. Hu, C. Wang, T. An, Y.D. Su, Q.N. Meng, et al., Effects of substrate bias on the preferred orientation, phase transition and mechanical properties for NbN films grown by direct current reactive magnetron sputtering, J. Appl. Phys. 104 (2008) 023527, http://dx.doi.org/10.1063/1.2956706.
[17] J.E. Alfonso, J. Buitrago, J. Torres, J.F. Marco, B. Santos, Influence of fabrication parameters on crystallization, microstructure, and surface composition of NbN thin films deposited by rf magnetron sputtering, J. Mater. Sci. 45 (2010) 5528–5533, http://dx.doi.org/10.1007/s10853-010-4612-3.
[18] K. Singh, A.C. Bidaye, A.K. Suri, Magnetron sputtered NbN films with Nb interlayer on mild steel, Int. J. Corros. 2011 (2011) 1–11, http://dx.doi.org/10.1155/2011/748168.
[19] N. Hayashi, I.H. Murzin, I. Sakamoto, M. Ohkubo, Single-crystal niobium nitride thin films prepared with radical beam assisted deposition, Thin Solid Films 259 (1995) 146–149, http://dx.doi.org/10.1016/0040-6090(94)06436-9.
[20] G. Cappuccio, U. Gambardella, A. Morone, S. Orlando, G. Parisi, Pulsed laser ablation of NbN/MgO/NbN multilayers, Appl. Surf. Sci. 109–110 (1997) 399–402, http://dx.doi.org/10.1016/S0169-4332(96)00758-1.
[21] Y. Dong, Y. Liu, J. Dai, G. Li, Superhard Nb–Si–N composite films synthesized by reactive magnetron sputtering, Appl. Surf. Sci. 252 (2006) 5215–5219, http://dx.doi.org/10.1016/j.apsusc.2005.08.007.
[22] M. Benkahoul, C.S. Sandu, N. Tabet, M. Parlinska-Wojtan, A. Karimi, F. Lévy, Effect of Si incorporation on the properties of niobium nitride films deposited by DC reactive magnetron sputtering, Surf. Coat. Technol. 188–189 (2004) 435–439, http://dx.doi.org/10.1016/j.surfcoat.2004.08.048.
[23] C.S. Sandu, M. Benkahoul, R. Sanjinés, F. Lévy, Model for the evolution of Nb–Si–N thin films as a function of SI content relating the nanostructure to electrical and mechanical properties, Surf. Coat. Technol. 201 (2006) 2897–2903, http://dx.doi.org/10.1016/j.surfcoat.2006.06.003.
[24] C.S. Sandu, R. Sanjinés, M. Benkahoul, F. Medjani, F. Lévy, Formation of

composite ternary nitride thin films by magnetron sputtering co-deposition, Surf. Coat. Technol. 201 (2006) 4083–4089, http://dx.doi.org/10.1016/j.surfcoat.2006.08.100.
[25] J. Wang, Z. Song, K. Xu, Influence of sputtering bias on the microstructure and properties of Nb–Si–N films, Surf. Coat. Technol. 201 (2007) 4931–4934, http://dx.doi.org/10.1016/j.surfcoat.2006.07.082.
[26] Z.X. Song, Y. Wang, C.J.F. Wang, C.L. Liu, K.W. Xu, The effect of N2 partial pressure on the properties of Nb–Si–N films by RF Reactive Magnetron Sputtering, Surf. Coat. Technol. 201 (2007) 5412–5415, http://dx.doi.org/10.1016/j.surfcoat.2006.07.047.
[27] J.J. Jeong, C.M. Lee, Effects of post-deposition annealing on the mechanical and chemical properties of the Si3N4/NbN multilayer coatings, Appl. Surf. Sci. 214 (2003) 11–19, http://dx.doi.org/10.1016/S0169-4332(03)00351-9.
[28] J.J. Jeong, S.K. Hwang, C. Lee, Hardness and adhesion properties of HfN/Si3N4 and NbN/Si3N4 multilayer coatings, Mater. Chem. Phys. 77 (2003) 27–33, http://dx.doi.org/10.1016/S0254-0584(01)00598-3.
[29] M. Wen, Q.N. Meng, C.Q. Hu, T. An, Y.D. Su, W.X. Yu, et al., Structure and mechanical properties of δ-NbN/SiNx and δ′-NbN/SiNx nano-multilayer films deposited by reactive magnetron sputtering, Surf. Coat. Technol. 203 (2009) 1702–1708, http://dx.doi.org/10.1016/j.surfcoat.2009.01.002.
[30] V.I. Ivashchenko, P.L. Scrynskyy, O.S. Lytvyn, O.O. Butenko, O.K. Sinelnichenko, L. Gorb, et al., Comparative investigation of NbN and Nb-Si-N films: experiment and theory, J. Superhard Mater. 36 (2014) 381–392, http://dx.doi.org/10.3103/S1063457614060033.
[31] U. Welzel, J. Ligot, P. Lamparter, A.C. Vermeulen, E.J. Mittemeijer, Stress analysis of polycrystalline thin films and surface regions by X-ray diffraction, J. Appl. Crystallogr. 38 (2005) 1–29, http://dx.doi.org/10.1107/S0021889804029516.
[32] J.D. Kamminga, T.H. De Keijser, R. Delhez, E.J. Mittemeijer, On the origin of stress in magnetron sputtered TiN layers, J. Appl. Phys. 88 (2000) 6332–6345.
[33] P. Giannozzi, S. Baroni, N. Bonini, M. Calandra, R. Car, C. Cavazzoni, et al., QUANTUM ESPRESSO: a modular and open-source software project for quantum simulations of materials, J. Phys. Condens. Matter 21 (2009) 395502, http://dx.doi.org/10.1088/0953-8984/21/39/395502.
[34] J.P. Perdew, K. Burke, M. Ernzerhof, Generalized gradient approximation made simple, Phys. Rev. Lett. 77 (1996) 3865–3868.
[35] D. Vanderbilt, Soft self-consistent pseudopotentials in a generalized eigenvalue formalism, Phys. Rev. B 41 (1990) 7892–7895, http://dx.doi.org/10.1103/PhysRevB.41.7892.
[36] S.R. Billeter, A. Curioni, W. Andreoni, Efficient linear scaling geometry optimization and transition-state search for direct wavefunction optimization schemes in density functional theory using a plane-wave basis, Comput. Mater. Sci. 27 (2003) 437–445, http://dx.doi.org/10.1016/S0927-0256(03)00043-0.
[37] V.I. Ivashchenko, S. Veprek, P.E.A. Turchi, V.I. Shevchenko, J. Leszczynski, L. Gorb, et al., First-principles molecular dynamics investigation of thermal and mechanical stability of the TiN(001)/AlN and ZrN(001)/AlN heterostructures, Thin Solid Films 564 (2014) 284–293, http://dx.doi.org/10.1016/j.tsf.2014.05.036.
[38] H.J. Monkhorst, J.D. Pack, Special points for brillouin-zone integrations, Phys. Rev. B 13 (1976) 5188–5192, http://dx.doi.org/10.1103/PhysRevB.13.5188.
[39] V.I. Ivashchenko, P.E.A. Turchi, A. Gonis, L.A. Ivashchenko, P.L. Skrynskii, Electronic origin of elastic properties of titanium carbonitride alloys, Metall. Mater. Trans. A 37 (2006) 3391–3396, http://dx.doi.org/10.1007/s11661-006-1031-9.
[40] E.I. Isaev, S.I. Simak, I.A. Abrikosov, R. Ahuja, Y.K. Vekilov, M.I. Katsnelson, et al., Phonon related properties of transition metals, their carbides, and nitrides: a first-principles study, J. Appl. Phys. 101 (2007) 123519, http://dx.doi.org/10.1063/1.2747230.
[41] V.I. Ivashchenko, S. Vepřek, First-principles molecular dynamics study of the thermal stability of the BN, AlN, SiC and SiN interfacial layers in TiN-based heterostructures: Comparison with experiments, Thin Solid Films. 545 (2013) 391–400, http://dx.doi.org/10.1016/j.tsf.2013.08.047.
[42] V. Ivashchenko, S. Veprek, A. Pogrebnjak, B. Postolnyi, First-principles quantum molecular dynamics study of TixZr1 – xN(111)/SiN y heterostructures and comparison with experimental results, Sci. Technol. Adv. Mater. 15 (2014) 025007, http://dx.doi.org/10.1088/1468–6996/15/2/025007.
[43] A.D. Pogrebnjak, A.A. Bagdasaryan, I.V. Yakushchenko, V.M. Beresnev, The structure and properties of high-entropy alloys and nitride coatings based on them, Russ. Chem. Rev. 83 (2014) 1027–1061, http://dx.doi.org/10.1070/RCR4407.
[44] A.D. Pogrebnjak, I.V. Yakushchenko, A.A. Bagdasaryan, O.V. Bondar, R. Krause-Rehberg, G. Abadias, et al., Microstructure, physical and chemical properties of nanostructured (Ti–Hf–Zr–V–Nb)N coatings under different deposition conditions, Mater. Chem. Phys. 147 (2014) 1079–1091, http://dx.doi.org/10.1016/j.matchemphys.2014.06.062.
[45] A.D. Pogrebnjak, D. Eyidi, G. Abadias, O.V. Bondar, V.M. Beresnev, O.V. Sobol, Structure and properties of arc evaporated nanoscale TiN/MoN multilayered systems, Int. J. Refract. Met. Hard Mater. 48 (2015) 222–228, http://dx.doi.org/10.1016/j.ijrmhm.2014.07.043.
[46] A.D. Pogrebnjak, V.M. Beresnev, Nanocoatings Nanosystems Nanotechnologies, BENTHAM SCIENCE PUBLISHERS 2012, http://dx.doi.org/10.2174/9781608054169112010l.
[47] M.F. Gozzi, E. Radovanovic, I.V.P. Yoshida, Si3N4/SiC nanocomposite powder from a preceramic polymeric network based on poly(methy lsilane) as the SiC precursor, Mater. Res. 4 (2001) 13–17, http://dx.doi.org/10.1590/S1516-14392001000100004.
[48] X.-J. Chen, V.V. Struzhkin, Z. Wu, R.E. Cohen, S. Kung, H. Mao, et al., Electronic stiffness of a superconducting niobium nitride single crystal under pressure, Phys. Rev. B 72 (2005) 094514, http://dx.doi.org/10.1103/PhysRevB.72.094514.
[49] G. Abadias, Stress and preferred orientation in nitride-based PVD coatings, Surf. Coat. Technol. 202 (2008) 2223–2235, http://dx.doi.org/10.1016/j.surfcoat.2007.08.029.
[50] A. Darlinski, J. Halbritter, On the identification of interface oxides and interface serration by ARXPS, Fresenius' Z. Für Anal. Chem. 329 (1987) 266–271, http://dx.doi.org/10.1007/BF00469154.
[51] G. Beamson, D. Briggs, High resolution monochromated X-ray photoelectron spectroscopy of organic polymers: A comparison between solid state data for organic polymers and gas phase data for small molecules, Mol. Phys. 76 (1992) 919–936, http://dx.doi.org/10.1080/00268979200101761.
[52] L. Yate, L. Emerson Coy, G. Wang, M. Beltrán, E. Díaz-Barriga, E.M. Saucedo, et al., Tailoring mechanical properties and electrical conductivity of flexible niobium carbide nanocomposite thin films, RSC Adv. 4 (2014) 61355–61362, http://dx.doi.org/10.1039/C4RA11292J.
[53] S. Hao, B. Delley, S. Veprek, C. Stampfl, Superhard nitride-based nanocomposites: role of interfaces and effect of impurities, Phys. Rev. Lett. 97 (2006) 086102, http://dx.doi.org/10.1103/PhysRevLett.97.086102.
[54] V.I. Ivashchenko, P.E.A. Turchi, E.I. Olifan, Phase stability and mechanical properties of niobium nitrides, Phys. Rev. B 82 (2010) 054109, http://dx.doi.org/10.1103/PhysRevB.82.054109.
[55] M. Chauhan, D.C. Gupta, Phase stability, ductility, electronic, elastic and thermo-physical properties of TMNs (TM=V, Nb and Ta): An ab initio high pressure study, Comput. Mater. Sci. 90 (2014) 182–195, http://dx.doi.org/10.1016/j.commatsci.2014.03.038.
[56] A.T. Asvini Meenaatci, R. Rajeswarapalanichamy, K. Iyakutti, Electronic structure, structural stability, mechanical and superconducting properties of group VB nitrides: A first principles study, Solid State Sci. 19 (2013) 36–44, http://dx.doi.org/10.1016/j.solidstatesciences.2013.02.004.
[57] B.D. Fulcher, X.Y. Cui, B. Delley, C. Stampfl, Hardness analysis of cubic metal mononitrides from first principles, Phys. Rev. B 85 (2012) 184106, http://dx.doi.org/10.1103/PhysRevB.85.184106.
[58] D. Holec, M. Friák, J. Neugebauer, P.H. Mayrhofer, Trends in the elastic response of binary early transition metal nitrides, Phys. Rev. B 85 (2012) 064101, http://dx.doi.org/10.1103/PhysRevB.85.064101.
[59] M.G. Brik, C.-G. Ma, First-principles studies of the electronic and elastic properties of metal nitrides XN (X=Sc, Ti, V, Cr, Zr, Nb), Comput. Mater. Sci. 51 (2012) 380–388, http://dx.doi.org/10.1016/j.commatsci.2011.08.008.
[60] T. Amriou, B. Bouhafs, H. Aourag, B. Khelifa, S. Bresson, C. Mathieu, FP-LAPW investigations of electronic structure and bonding mechanism of NbC and NbN compounds, Phys. B Condens. Matter 325 (2003) 46–56, http://dx.doi.org/10.1016/S0921-4526(02)01429-1.
[61] J.O. Kim, J.D. Achenbach, P.B. Mirkarimi, M. Shinn, S.A. Barnett, Elastic constants of single-crystal transition-metal nitride films measured by line-focus acoustic microscopy, J. Appl. Phys. 72 (1992) 1805, http://dx.doi.org/10.1063/1.351651.